


Covalent Organic Frameworks **Hot Paper**


Geomimetic Hydrothermal Synthesis of Polyimide-Based Covalent Organic Frameworks

Taehyung Kim, Se Hun Joo, Jintaek Gong, Sungho Choi, Ju Hong Min, Yongchul Kim, Geunsik Lee, Eunji Lee, Soojin Park, Sang Kyu Kwak, Hee-Seung Lee, and Byeong-Su Kim*

Abstract: Despite its abundance, water is not widely used as a medium for organic reactions. However, under geothermal conditions, water exhibits unique physicochemical properties, such as viscosity and a dielectric constant, and the ionic product become similar to those of common organic solvents. We have synthesized highly crystalline polyimide-based covalent organic frameworks (PICs) under geomimetic hydrothermal conditions. By exploiting triphenylene-2,3,6,7,10,11-hexacarboxylic acid in combination with various aromatic diamines, PICs with various pore dimensions and crystallinities were synthesized. XRD, FT-IR, and DFT calculations revealed that the solubility of the oligomeric intermediates under hydrothermal conditions affected the stacking structures of the crystalline PICs. Furthermore, the synthesized PICs demonstrate promising potential as an anode material in lithium-ion batteries owing to its unique redox-active properties and high surface area.

Introduction

Natural zeolites are formed during the deposition of natural ores. Such processes take place in veins of the Earth's crust that are filled with high-temperature water delimited with solid rocks, thus creating highly dynamic systems (i.e., high temperature and pressure) for the synthesis of highly crystalline minerals.^[1–3] Inspired by this geothermal process, hydrothermal reaction occurring under high temperature and pressure can offer a convenient access toward the synthesis of a range of crystalline materials, such as gemstones, zeolites, and carbonaceous materials.^[4] In addition, the use of hydrothermal reactions is promising for the synthesis of organic materials because of its simplicity, environmental sustainability, and low cost.^[5–9]

Conventional organic reactions do not typically occur in water under ambient conditions; however, under hydrothermal conditions, the physicochemical properties of water change significantly as a result of the breakage of the hydrogen-bonded water network.^[10] For example, the density and viscosity of water decrease significantly under hydrothermal conditions, thus affecting diffusion-controlled chemical reactions. Furthermore, the dielectric constant of water changes continuously and may even match that of common organic solvents under ambient conditions.^[11] More importantly, the ionic product of water (K_w) increases with increasing temperature, thus accelerating the rate of acid- and base-catalyzed reactions.^[12]

Covalent organic frameworks (COFs) are highly ordered multidimensional polymeric networks that are synthesized by connecting organic building blocks with covalent linkages.^[13] Owing to their outstanding properties such as high crystallinity and porosity with uniform pore size, they have attracted widespread interest for diverse potential applications, including batteries,^[14–17] supercapacitors,^[18] catalysts,^[19–21] gas storage,^[22] separation membranes,^[23,24] and sensors.^[25,26] The high crystallinity of COFs can be attributed to the formation of reversible bonds during polymerization, which allows for structural error correction. Thus, many dynamic chemical reactions have been employed for the formation of COFs, such as boronic acid trimerization,^[13] Schiff base reaction,^[14] boronate ester formation,^[27] and nitrile trimerization.^[28] However, these dynamic bonds are often susceptible to hydrolysis. Alternatively, amide bonds have recently been utilized as linkages for the synthesis of COFs with enhanced chemical stability, yet with a relatively low crystallinity.^[29,30]

As one of the most important classes of high-performance polymers, polyimide (PI) is generally synthesized using an

[*] T. Kim, B.-S. Kim

Department of Chemistry, Yonsei University
 Seoul 03722 (Republic of Korea)
 E-mail: bskim19@yonsei.ac.kr

T. Kim, S. H. Joo, Prof. S. K. Kwak
 School of Energy and Chemical Engineering
 Ulsan National Institute of Science and Technology (UNIST)
 Ulsan 44919 (Republic of Korea)



J. Gong, Prof. H.-S. Lee
 Center for Multiscale Chiral Architectures and Department of Chemistry
 Korea Advanced Institute of Science and Technology (KAIST)
 Daejeon 34141 (Republic of Korea)

S. Choi, Prof. S. Park

Division of Advanced Material Science, Department of Chemistry
 Pohang University of Science and Technology (POSTECH)
 Pohang 37673 (Republic of Korea)

J. H. Min, Prof. E. Lee
 School of Materials Science and Engineering
 Gwangju Institute of Science and Technology (GIST)
 Gwangju 61005 (Republic of Korea)

Y. Kim, Prof. G. Lee
 Department of Chemistry
 Ulsan National Institute of Science and Technology (UNIST)
 Ulsan 44919 (Republic of Korea)

 Supporting information and the ORCID identification number(s) for the author(s) of this article can be found under:
 <https://doi.org/10.1002/anie.202113780>

imidization reaction between anhydride and amine precursors. Although PI exhibits excellent thermal stability, mechanical performance, chemical resistance, and redox-active properties,^[31] there are few studies on PI-based COFs because the formation of imide bonds is favored over the deformation, thus limiting their capability to achieve long-range-ordered crystalline PI networks. As such, most previous studies have employed solvothermal methods using a combination of toxic organic solvents and catalysts in a closed vessel with a low internal pressure to facilitate the nucleation and crystallization of the PI-based COFs; under these conditions, the reversibility of COF formation is maintained and the equilibrium reaction yielding water as a byproduct is controlled (Supporting Information, Table S1).^[23,32–37] Recently, Lotsch and co-workers reported a new synthetic method (i.e., ionothermal synthesis) for PI-COFs using ZnCl_2 as reaction media free of toxic solvents.^[38] Although this protocol provides a new perspective over conventional solvothermal reactions, it is still highly desirable to search for alternative eco-friendly reaction media.

Inspired by the recent pioneering works by Unterlass and co-workers in the synthesis of crystalline PIs using hydrothermal polymerization,^[39,40] herein, we report the first synthesis of highly crystalline PI-based COFs (hereafter, denoted as PIC) via geomimetic hydrothermal synthesis without using a catalyst or toxic solvents. In particular, triphenylene-2,3,6,7,10,11-hexacarboxylic acid (TPHCA) was designed as a C_3 -type anhydride precursor to facilitate the selective formation of imide bonds. In addition, three aromatic diamines (i.e., *p*-phenylenediamine (Ph), 4,4'-diaminobiphenyl (Dp), and 4,4'-diamino-*p*-terphenyl (Tp)) were used to synthesize PICs having various pore dimensions and crystallinity (Figure 1). Furthermore, density functional theory-based tight binding (DFTB) calculations revealed that the type of diamine affected the stacking behavior of the crystalline PICs. Moreover, *ex situ* X-ray diffractometry (XRD) and Fourier-transform infrared (FT-IR) spectroscopy analyses suggested that the solubility of the oligomer intermediates affected the mechanism of formation of the PICs synthesized under hydrothermal conditions. By taking advantage of the unique redox-active properties of the imide linkages as well as the large surface area, PIC was further examined for its potential as an active organic anode material for lithium-ion batteries.

Early attempt in the synthesis of PICs via a hydrothermal method using mellitic acid led to a limited success due to the competition between the formation of amide and imide bonds (i.e., mono- vs. bi-functional).^[41] This suggests that it is critical to ensure the selectivity for imide bond formation for the successful synthesis of PICs. Therefore, in this study, a new hexacarboxylic acid precursor for the hydrothermal synthesis of PICs was designed by introducing a phenyl group between the central core and each dicarboxylic acid group to prevent the random reaction between the carboxylic acids and amines. The C_3 -type hexacarboxylic acid precursor (i.e., TPHCA) was synthesized via a modified literature method^[42] starting from hexamethylbenzene in four steps with an overall yield of 10.4% (Supporting Information, Figure S1). The intermediates and the final product were successfully characterized

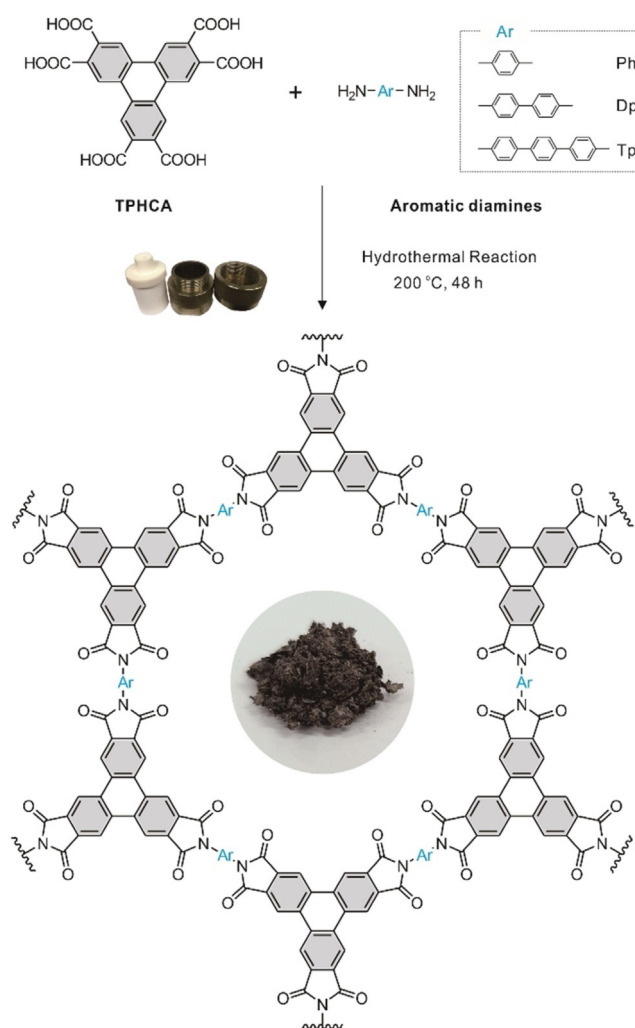


Figure 1. Illustration of the hydrothermal synthesis of polyimide-based COFs (PICs) by reacting triphenylene-2,3,6,7,10,11-hexacarboxylic acid (TPHCA) with various aromatic diamines (i.e., *p*-phenylenediamine (Ph), 4,4'-diaminobiphenyl (Dp), and 4,4'-diamino-*p*-terphenyl (Tp)). Inset: the obtained PIC-Ph powder.

using ^1H - and ^{13}C -NMR, FT-IR spectroscopy, and LC-MS spectrometry (Figures S2–S5).

Results and Discussion

Synthesis and characterization of PICs. PIC-Ph and PIC-Dp were synthesized by the hydrothermal imidization reaction of TPHCA with Ph and Dp, as shown in Figure 1. Characteristic peaks were observed in the FT-IR spectra of the samples at 1718 and 1775 cm^{-1} , corresponding to the symmetric and asymmetric vibrations of a carbonyl group in a cyclic imide, respectively. Additional peaks were observed at 1350, 1356, and 1363 cm^{-1} , which can be attributed to the stretching vibrations of the cyclic imide moiety. Furthermore, the peaks corresponding to the carboxylic acid of the precursor TPHCA at 1693 cm^{-1} and the amide bond of the intermediate at 1660 cm^{-1} were not observed, indicating full imidization to yield the desired PICs (Figure 2a,b). In

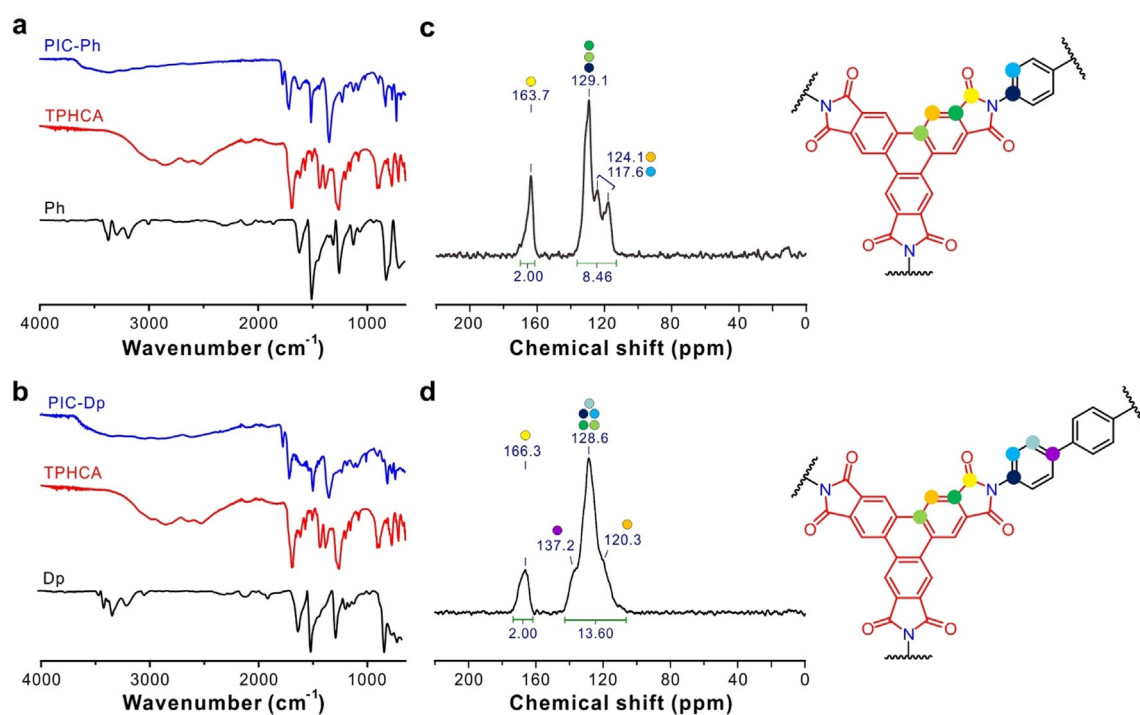


Figure 2. Characterization of PIC-Ph and PIC-Dp. a,b) FT-IR spectra of PIC-Ph (a) and PIC-Dp (b). c,d) Solid-state CP-MAS ^{13}C -NMR spectra of PIC-Ph (c) and PIC-Dp (d) with the corresponding chemical structures of the repeating units.

parallel, solid-state cross-polarization magic-angle-spinning (CP-MAS) ^{13}C -NMR spectra indicate the presence of the carbonyl carbon of the imide ring, as shown by peaks at 163.7 and 166.3 ppm, and aromatic carbons in overlapping peaks from 110 to 140 ppm with corresponding integral values consistent with the suggested repeating unit structures (Figure 2c,d; Table S2). Taken together, these results suggested that successful formation of PICs free of amide and amic acid intermediates.

The crystal structures of the PICs were determined using powder X-ray diffraction (PXRD) analysis with $\text{Cu-K}\alpha$ radiation (Figure 3a,b). As the COF structures consist of not only 2-dimensional (2D) individual linkages but also 3-dimensional (3D) stacking of the 2D layers, the characteristics of the COFs, such as porosity, electronic, and optical properties, were influenced by the 3D stacking structures^[43,44] in concert with the concept of nanoarchitectonics.^[45]

DFTB calculations were employed to investigate the detailed structure of the synthesized PICs, and four possible 3D stacking structures were generated for the 2D PICs using the 3OB Slater-Koster atomic parameters. These structures include eclipsed (AA and AA') and staggered (AB and ABC) stacking structures (Figure 3a–e; Figure S6, Table S3). The potential energy surfaces generated by scanning the potential energy as the monolayers were shifted (Figure S7) revealed that the AA'-eclipsed stacking structure was the most thermodynamically stable structure in PIC-Ph (Figure 3c), in good agreement with the sharp peaks observed at 3.60° , 6.16° , 7.18° , 9.36° , 12.76° , and 25.38° (Figure 3a). Each peak was assigned to more than two different facets because of the slightly tilted structure of the *Cmcm* space group (Table S4).

In contrast to PIC-Ph, in which the AA' stacking structure was predominant, no peak corresponding to the (100) peak of the eclipsed structure below 3° was observed in the PXRD pattern of PIC-Dp. In addition, the peak observed at approximately 15° suggests that PIC-Dp exhibited a staggered structure; however, the potential energy surface indicated that the AA' stacking was the most thermodynamically stable structure in PIC-Dp (Figure 3b,d; Figure S6). The overall peak patterns in the experimental results are consistent with those of the AB-staggered structure, except for the (100) plane, which was not observed in the XRD patterns due to the detection limit of the instrument. In contrast, the small-angle X-ray scattering (SAXS) pattern collected in the low-angle range revealed a peak at 2.35° that can be assigned to the (100) plane (Figure S8).

Owing to the different stacking structures, PIC-Ph and PIC-Dp had different porosity and chemical stability. First, the porosity of PIC-Ph and PIC-Dp was examined using N_2 -sorption isotherms at 77 K. PIC-Ph exhibited type-IV isotherm adsorption/desorption curves. In addition, a sharp adsorption nitrogen uptake was observed below $P/P_0 = 0.05$, which corresponds to the presence of micropores. Furthermore, the lack of hysteresis in the adsorption/desorption curves suggests that the reversible adsorption/desorption process occurred through similar mechanisms. The Brunauer-Emmett-Teller (BET) surface area of PIC-Ph was determined to be $669 \text{ m}^2 \text{ g}^{-1}$, which is similar to the value reported previously for PICs (Figure S9a).^[34,46] In contrast, PIC-Dp exhibited type-II isotherm adsorption/desorption curves, which indicates a macroporous structure without micropores. In addition, the BET surface area of PIC-Dp was $125 \text{ m}^2 \text{ g}^{-1}$, which is relatively low compared to that of PIC-Ph due to the

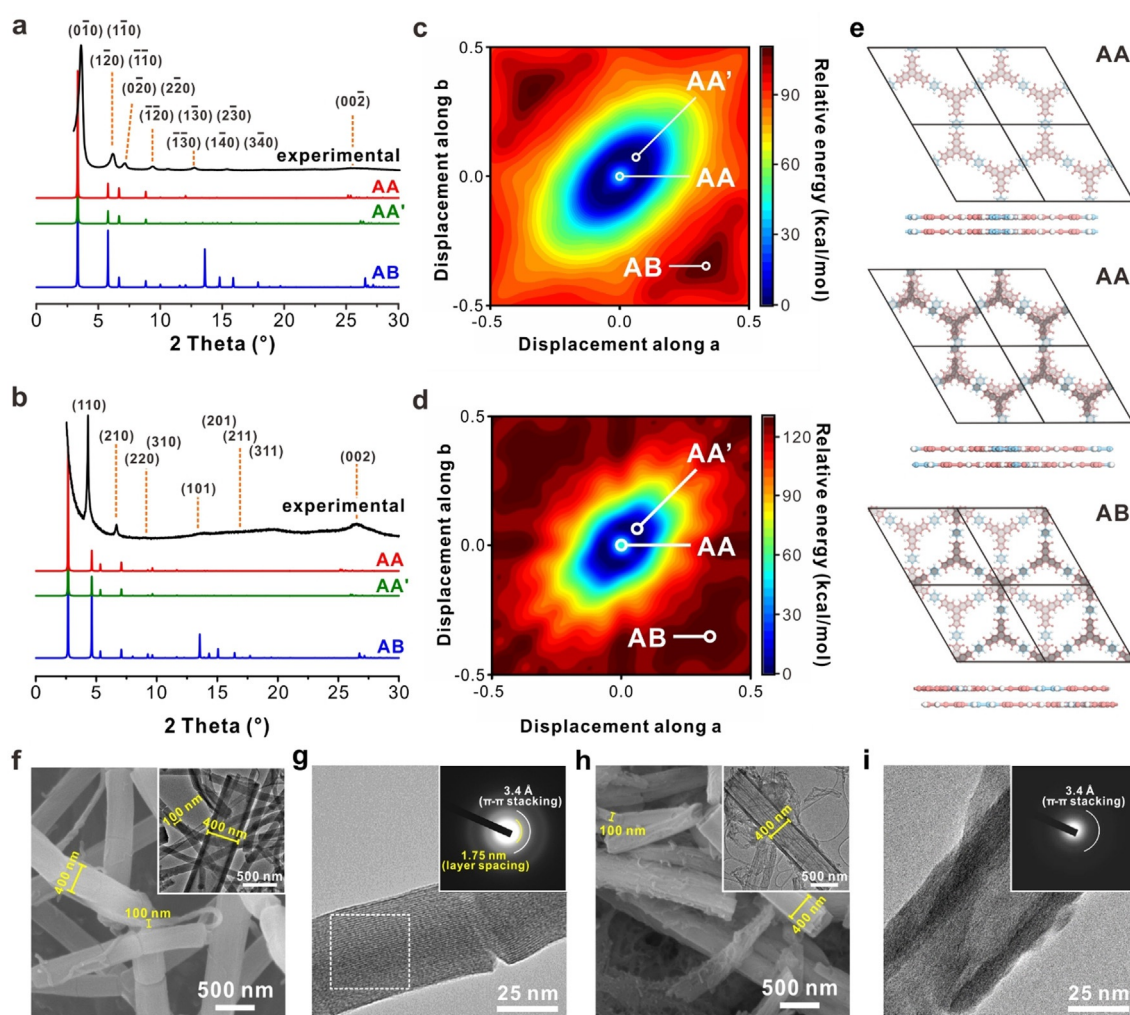


Figure 3. Synchrotron PXRD patterns of a) PIC-Ph and b) PIC-Dp (black) and calculated patterns of the AA-eclipsed (red), AA'-eclipsed (green), and AB-staggered (blue) structures. c,d) Potential energy surface of PIC-Ph and PIC-Dp with calculated stacking patterns labeled. The x and y axes correspond to the fractional coordinates. e) Top and side views of the calculated AA, AA', and AB-stacking structures of the PIC-Ph layers. SEM images of f) PIC-Ph and h) PIC-Dp (insets: the TEM images). High-resolution TEM images of g) PIC-Ph and i) PIC-Dp (insets: SAED patterns).

reduced interlayer distance of the staggered structure (Figure S9b). In addition, the chemical stability was investigated by subjecting the PICs to water, 5 M HCl, and 5 M NaOH for 7 days.

The morphology of the as-prepared PICs was investigated by scanning electron microscopy (SEM) and transmission electron microscopy (TEM). Interestingly, a fibrous morphology comprising fibers having a diameter of approximately 100 nm was observed in the samples, which could be attributed to the stacking of the assembled PICs, and a tubular morphology with a diameter of 400 nm and wall thickness of 80 nm was observed (Figure 3 f,h). These tubular structures are formed of assemblies of individual fibers. Furthermore, high-resolution TEM and selected area electron diffraction (SAED) revealed a π - π stacking distance of 3.4 Å for both PICs, which is well matched with the interlayer distance for PIC crystal structures (3.40 Å for PIC-Ph and 3.33 Å for PIC-Dp, respectively) (Figure 3 g,i). In addition, the fast Fourier transforms (FFT) of the diffraction patterns confirmed that PIC-Ph has a layered structures with a *d*-spacing of 1.75 nm,

corresponding to the length of the hexagonal base repeating unit of the PIC-Ph (Figures S10 and S11). However, this layered structure was not observed in PIC-Dp, indicating the absence of a periodic arrangement. The XRD and SEM analyses revealed that aging the PICs for 7 days in aqueous solutions had no effect on their crystallinity and morphology even under highly acidic conditions (Figures S12 and S13). However, the PICs exhibited different chemical stability under alkaline conditions. For example, the structural integrity of PIC-Ph was not preserved in 5 M NaOH, as observed for other PI-based materials (Figure S12). In contrast, there were no noticeable changes in the crystallinity and morphology of PIC-Dp under alkaline conditions (Figure S13). This additional chemical stability of PIC-Dp could be attributed to its relatively lower porosity, which limited the migration of the alkaline solution into the structure. In addition to the enhanced chemical stability of the prepared PICs, we evaluated their thermal stability. A negligible weight loss was observed in the thermogravimetric analysis (TGA) curves of PIC-Ph and PIC-Dp, even at 590 and 595 °C,

respectively, indicating the superior thermal stability of the PICs synthesized in this study (Figure S14).

Formation Mechanism of the PICs. It has been previously suggested that salts of the precursors are first formed as intermediates during the hydrothermal polymerization of crystalline PI through a series of dissolution-polymerization-crystallization processes.^[37] On the basis of this mechanism, we investigated the detailed reaction process by analyzing the intermediates through *ex situ* XRD and FT-IR to elucidate the origin of the difference in the stacking structures of PIC-Ph and PIC-Dp (Figures S15 and S16). For this purpose, we performed the hydrothermal polymerization of the respective PICs for different durations (10 min, 30 min, 1 h, and 6 h) and characterized the intermediates without additional purification processes.

According to the XRD results of PIC-Ph, crystalline intermediates were observed from the appearance of the new crystalline peaks from 5° to 15° beginning from 30 min of hydrothermal polymerization (Figure S15). In addition, *ex situ* FT-IR spectroscopy revealed that these crystalline intermediates were precursor salts, as shown by the aromatic NH₃⁺ peaks, which were gradually consumed with TPHCA (Figure S16). Upon increasing the reaction time, these intermediates were gradually transformed into a 2D interconnected PIC-Ph layer, which in turn led to the AA'-eclipsed stacking structure, as evidenced by the appearance of a peak corresponding to the (010) and (110) planes at 3.60° (Figure S15a,b).

As observed for PIC-Ph, peaks consistent with the formation and transformation of crystalline salt intermediates, such as the appearance of aromatic NH₃⁺ peaks, were observed in the XRD patterns and FT-IR spectra of PIC-Dp (Figures S15 and S16). In the initial stages of the reaction, the intensity of the imide bond peak increased with increase in the consumption of NH₃⁺, suggesting that PIC-Dp was constructed from the salt intermediate. After 30 min, the intensity of the imide bonds reached saturation, whereas the carboxylic acid peaks of TPHCA (1693 cm⁻¹) and aromatic NH₃⁺ peaks (2920 and 2600 cm⁻¹) were retained. This observation demonstrates the immature precipitation of PIC-Dp from the oligomeric intermediates with reduced aqueous solubility, which was followed by the independent formation of additional PIC-Dp from the precursor solution.

Based on these results, we propose the following mechanistic framework for the hydrothermal synthesis of PICs. Briefly, the solubility of the oligomeric structure affected the reaction pathway of the 2D hexagonal PICs during the development of the 3D stacking structure (i.e., thermodynamic pathway for PIC-Ph and kinetic pathway for PIC-Dp) (Figure 4). More specifically, in the case of PIC-Ph, soluble oligomeric structures were formed from the crystalline intermediates and acted as seeds for the growth of PIC-Ph with long-range order through a nucleation/growth mechanism under homogeneous reaction conditions (Figure 4a). With the growth of the 2D layer, the most thermodynamically stable structure, the AA'-eclipsed structure of PIC-Ph, was formed, which was resulted from π - π interactions between the aromatic rings (Figure 4b,c).

On the other hand, insoluble oligomeric intermediates were formed in the case of PIC-Dp due to the lower solubility of the biphenyl ring, thus limiting the long-range growth of the 2D structure as they precipitate out. Consequently, PIC-Dp formed a kinetically stable AB-staggered stacking structure rather than a thermodynamically stable eclipsed stacking structure.

Moreover, among the staggered structures, the ABC stacking structure exhibited higher thermodynamic stability than the AB-stacking structure with interlayer space packing, which was induced by the relaxation of the individual 2D layers (Figure S17, Table S5). However, there are water molecules between the PIC layers owing to the hydrogen bonding between the imide and water during the formation of PIC-Dp, thus interfering with the interlayer packing. Consequently, the AB-staggered stacking was more predominant than the ABC-staggered stacking, which did not exhibit the relaxation of the 2D layers (Figure 4c).

To confirm the proposed mechanism, the hydrothermal polymerization process was extended to the synthesis of PIC-Tp using 4,4''-diamino-*p*-terphenyl (Tp) as a precursor (Figure 1), and the chemical structure of the prepared PIC-Tp was investigated using FT-IR and solid-state CP-MAS ¹³C-NMR spectroscopy. The FT-IR analysis revealed that PIC-Tp has a cyclic imide structure, and the repeating units consisting of carbonyl and aromatic carbons were assigned by solid-state CP-MAS ¹³C-NMR (Figure S18, Table S2).

Despite the successful synthesis of PIC-Tp, it was difficult to individually assign the crystal structure of PIC-Tp by XRD owing to the presence of residual Tp (as shown by the peak at 20° in Figure S18). This suggests that the longer aromatic groups in the Tp precursor, which has limited aqueous solubility, resulted in its physical trapping within the PIC-Tp structure, particularly in the initial stages of oligomeric intermediate growth. In addition, owing to the presence of the residual Tp precursor in the PIC-Tp structure, PIC-Tp exhibited a low BET surface area of 54 m²g⁻¹ and a TGA weight loss at approximately 200°C, consistent with the degradation temperature of the residual Tp precursor, although the peak at 605°C suggests the thermal stability of PIC-Tp (Figures S9 and S14).

Application of PICs. To utilize the unique redox-active property of the imide linkage and porosity of PIC, PIC-Ph was examined as an anode material for lithium-ion batteries (LIBs) (Figure 5). Prior to application in the LIB system, the theoretical capacity of PIC-Ph was calculated using DFT calculation. It was found that the redox-active carbonyl groups of imide bonds in the unit cell of PIC-Ph can be oxidized through the lithiation process by 12 lithium ions, resulting in a specific capacity of 294 mAh g⁻¹. Moreover, the benzene ring in the PIC-Ph was identified as another redox-active group that could be oxidized at approximately 0.19 V (vs. Li/Li⁺). As a result, lithium ions first reacted with the carbonyl groups in the imide (i.e., 12 lithium ions per unit cell) and subsequently with three benzene units in the unit cell of PIC-Ph (i.e., a total of 30 lithium ions per unit cell). This leads PIC-Ph to achieve a high theoretical specific capacity of 736.6 mAh g⁻¹, approximately two times higher than that of commercial graphite anodes (372 mAh g⁻¹) (Figure S19).

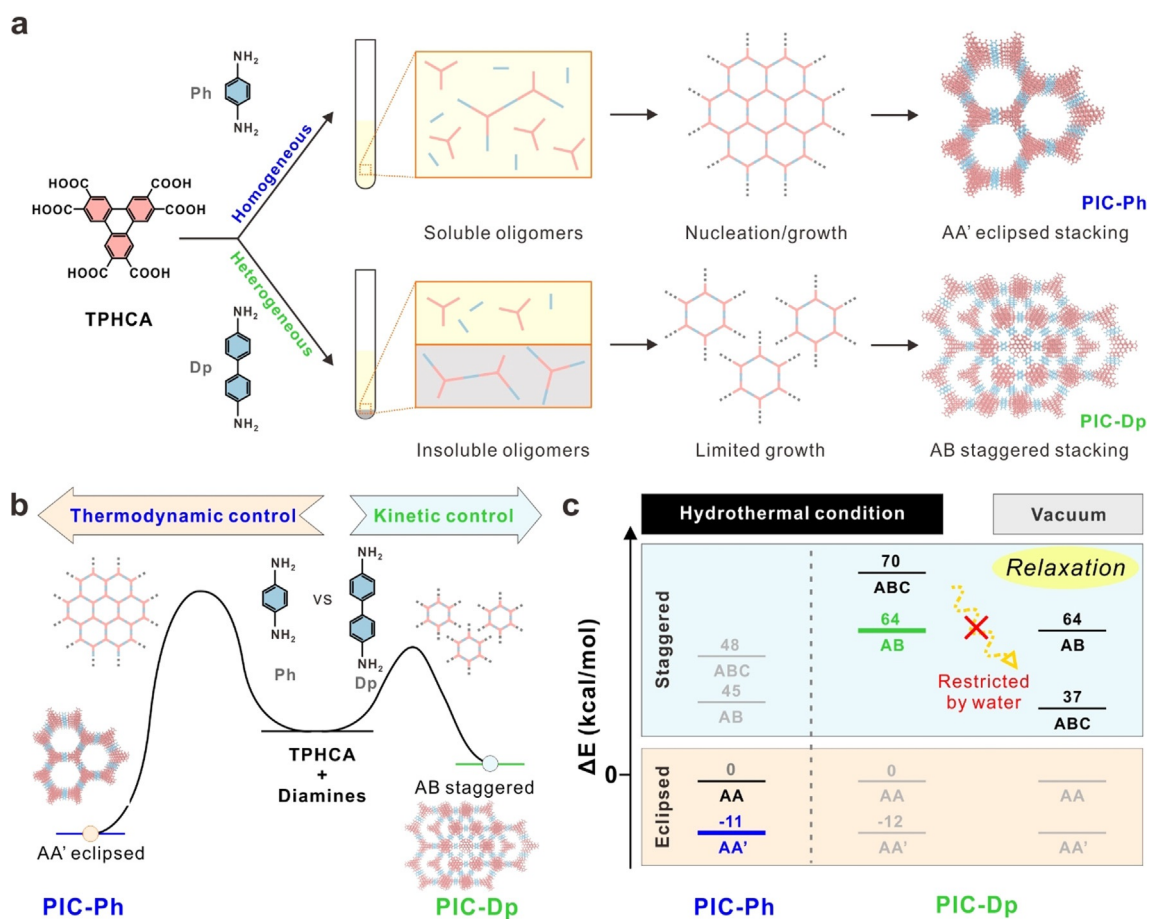


Figure 4. Illustration of the a) proposed reaction pathways and b) potential energy diagram: thermodynamic pathway of PIC-Ph and kinetic pathway of PIC-Dp. c) Representation of the relative energy levels of each stacking structure of the PICs.

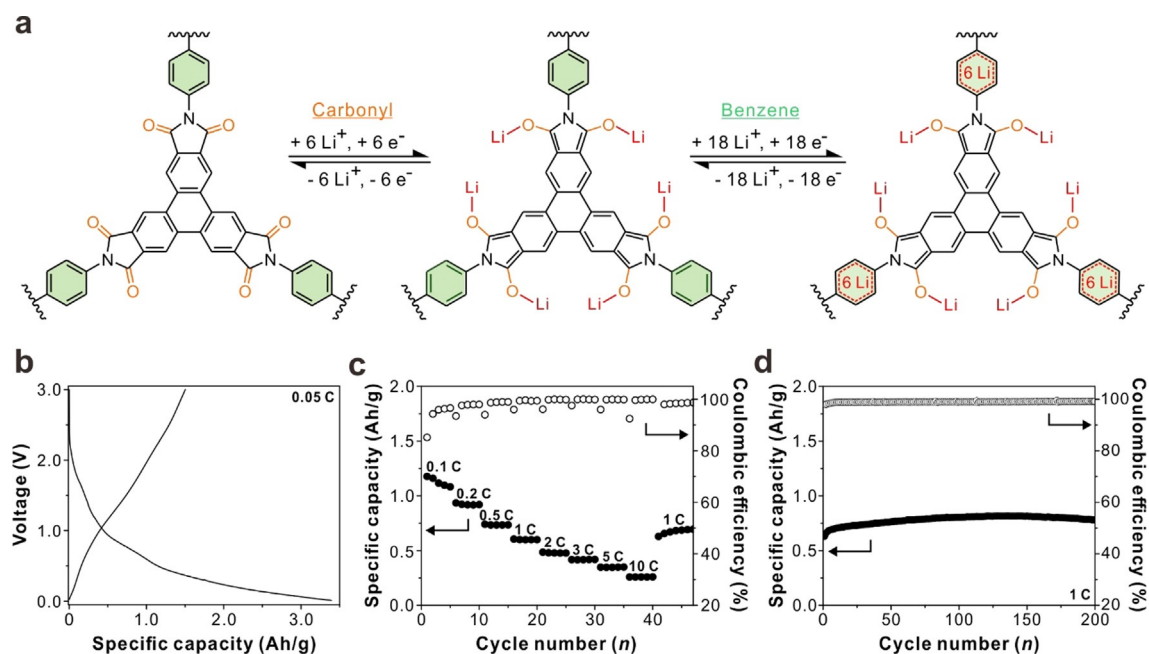


Figure 5. a) The application of PIC-Ph as an anode material during lithiation/delithiation. b–d) Electrochemical properties of the PIC-Ph electrode. Voltage profile of the first cycle at 0.05 C (b), rate capability at various C-rates and the corresponding coulombic efficiency (c), and cycle retention at 1 C after the rate capability tests and the coulombic efficiency (d). The open and closed circles correspond to the specific capacity and coulombic efficiency, respectively.

Based on the promising theoretical specific capacity of PIC-Ph, we performed electrochemical analysis as an anode in the conventional LIB system. As shown in Figure 5b, the electrode consisting of PIC-Ph delivered a specific capacity of $1502.0 \text{ mAh g}^{-1}$ with an initial coulombic efficiency of 44.3% in the first cycle (0.05 C). The electrode yielded a slightly lower initial coulombic efficiency and a higher specific capacity than the theoretical value. This can be attributed to solid electrolyte interphase formation and the adsorption/desorption reaction of lithium ions during the charge/discharge process in both the conductive materials and PIC-Ph owing to the large surface area and porous structure of PIC-Ph. Specifically, PIC-Ph demonstrated a specific capacity of 1116.2, 599.1, and 258.8 mAh g^{-1} at 0.1, 1.0, and 10 C, respectively, with a good rate capability compared to those of other organic-based anode materials (Figure 5c). Furthermore, it showed durable cycle retention with a reversible capacity of 691.9 mAh g^{-1} and an average coulombic efficiency of 99.1% at 1.0 C for 200 cycles (Figure 5d).

Conclusion

In summary, we synthesized highly crystalline PICs via a geomimetic hydrothermal polymerization method for the first time. TPHCA was used as an anhydride precursor in combination with three aromatic diamine precursors, Ph, Dp, and Tp, to afford PICs with various pore dimensions and crystallinity. Most importantly, we found that the solubility of the oligomeric structures affected the crystalline structures of the prepared PICs, particularly the 3D stacking structures. The soluble oligomers followed the nucleation-growth mechanism as they acted as seeds for the long-range growth of the PIC structure, for which the eclipsed structure was the most thermodynamically stable. In contrast, the precipitation of oligomeric intermediates limited the growth of the 2D PIC layers, thus making the staggered structure the most kinetically accessible structure. Finally, by taking advantage of the redox-active properties with porosity, PIC-Ph was applied as an active anode for LIBs. The PIC-Ph delivered a specific capacity of 691.9 mAh g^{-1} at 1.0 C with long-cycling stability for 200 cycles. We anticipate that this geomimetic hydrothermal method will enable eco-friendly synthesis of highly ordered organic materials.

Acknowledgements

This work was supported by the National Research Foundation of Korea (NRF-2021R1A2C3004978 and NRF-2018R1A5A1025208). The synchrotron powder X-ray diffraction data for structural analysis were collected from the 9B beamline at the Pohang Accelerator Laboratory (Pohang, Republic of Korea). S.K.K. acknowledges financial support from the C1 Gas Refinery Program through the National Research Foundation of Korea (NRF) funded by the Ministry of Science and ICT (NRF-2018M3D3A1A01055761). S.K.K. and G.L. acknowledge the computational calculations supported by the National Supercomputing Center with super-

computing resources including technical support (KSC-2021-CRE-0125 and KSC-2021-CRE-0188), UNIST-HPC, and UNIST supercomputing center.

Conflict of Interest

The authors declare no conflict of interest.

Keywords: hydrothermal reactions · oligomers · organic anodes · polyimides

- [1] M. Choi, H. S. Cho, R. Srivastava, C. Venkatesan, D.-H. Choi, R. Ryoo, *Nat. Mater.* **2006**, *5*, 718–723.
- [2] K. Na, M. Choi, W. Park, Y. Sakamoto, O. Terasaki, R. Ryoo, *J. Am. Chem. Soc.* **2010**, *132*, 4169–4177.
- [3] X. Bu, P. Feng, T. E. Gier, D. Zhao, G. D. Stucky, *J. Am. Chem. Soc.* **1998**, *120*, 13389–13397.
- [4] C. S. Cundy, P. A. Cox, *Chem. Rev.* **2003**, *103*, 663–702.
- [5] B. Baumgartner, A. Svirikova, J. Bintinger, C. Hametner, M. Marchetti-Deschmann, M. M. Unterlass, *Chem. Commun.* **2017**, *53*, 1229–1232.
- [6] M. J. Taublaender, F. Glöcklhofer, M. Marchetti-Deschmann, M. M. Unterlass, *Angew. Chem. Int. Ed.* **2018**, *57*, 12270–12274; *Angew. Chem.* **2018**, *130*, 12450–12454.
- [7] M. J. Taublaender, S. Mezzavilla, S. Thiele, F. Glöcklhofer, M. M. Unterlass, *Angew. Chem. Int. Ed.* **2020**, *59*, 15050–15060; *Angew. Chem.* **2020**, *132*, 15160–15171.
- [8] J. Chu, X. Li, Q. Li, J. Ma, B. Wu, X. Wang, R. Zhang, M. Gong, S. Xiong, *High Perform. Polym.* **2020**, *32*, 258–267.
- [9] F. Amaya-García, M. Caldera, A. Koren, S. Kubicek, J. Menche, M. M. Unterlass, *ChemSusChem* **2021**, *14*, 1853–1863.
- [10] N. Akiya, P. E. Savage, *Chem. Rev.* **2002**, *102*, 2725–2750.
- [11] M. Uematsu, E. U. Frank, *J. Phys. Chem. Ref. Data* **1980**, *9*, 1291–1306.
- [12] W. L. Marshall, E. U. Franck, *J. Phys. Chem. Ref. Data* **1981**, *10*, 295–304.
- [13] A. P. Côté, A. I. Benin, N. W. Ockwig, M. O’Keeffe, A. J. Matzger, O. M. Yaghi, *Science* **2005**, *310*, 1166–1170.
- [14] S. Wang, Q. Wang, P. Shao, Y. Han, X. Gao, L. Ma, S. Yuan, X. Ma, J. Zhou, X. Feng, B. Wang, *J. Am. Chem. Soc.* **2017**, *139*, 4258–4261.
- [15] H. Zhang, W. Sun, X. Chen, Y. Wang, *ACS Nano* **2019**, *13*, 14252–14261.
- [16] E. Vitaku, C. N. Gannett, K. L. Carpenter, L. Shen, H. D. Abruña, W. R. Dichtel, *J. Am. Chem. Soc.* **2020**, *142*, 16–20.
- [17] X. Li, Q. Hou, W. Huang, H.-S. Xu, X. Wang, W. Yu, R. Li, K. Zhang, L. Wang, Z. Chen, K. Xie, K. P. Loh, *ACS Energy Lett.* **2020**, *5*, 3498–3506.
- [18] A. Halder, M. Ghosh, A. Khayum M, S. Bera, M. Addicoat, H. S. Sasmal, S. Karak, S. Kurungot, R. Banerjee, *J. Am. Chem. Soc.* **2018**, *140*, 10941–10945.
- [19] T. Sick, A. G. Hufnagel, J. Kampmann, I. Kondofersky, M. Calik, J. M. Rotter, A. Evans, M. Döblinger, S. Herbert, K. Peters, D. Böhm, P. Knochel, D. D. Medina, D. Fattakhova-Rohlfing, T. Bein, *J. Am. Chem. Soc.* **2018**, *140*, 2085–2092.
- [20] H. Li, Q. Pan, Y. Ma, X. Guan, M. Xue, Q. Fang, Y. Yan, V. Valtchev, S. Qiu, *J. Am. Chem. Soc.* **2016**, *138*, 14783–14788.
- [21] X. Han, Q. Xia, J. Huang, Y. Liu, C. Tan, Y. Cui, *J. Am. Chem. Soc.* **2017**, *139*, 8693–8697.
- [22] S. Yu, J. Mahmood, H. Noh, J. Seo, S. Jung, S. Shin, Y. Im, I. Jeon, J. Baek, *Angew. Chem. Int. Ed.* **2018**, *57*, 8438–8442; *Angew. Chem.* **2018**, *130*, 8574–8578.

- [23] S. Zhang, Y. Zheng, H. An, B. Aguila, C. Yang, Y. Dong, W. Xie, P. Cheng, Z. Zhang, Y. Chen, S. Ma, *Angew. Chem. Int. Ed.* **2018**, *57*, 16754–16759; *Angew. Chem.* **2018**, *130*, 16996–17001.
- [24] Z. Wang, S. Zhang, Y. Chen, Z. Zhang, S. Ma, *Chem. Soc. Rev.* **2020**, *49*, 708–735.
- [25] G. Das, B. P. Biswal, S. Kandambeth, V. Venkatesh, G. Kaur, M. Addicoat, T. Heine, S. Verma, R. Banerjee, *Chem. Sci.* **2015**, *6*, 3931–3939.
- [26] L. Ascherl, E. W. Evans, J. Gorman, S. Orsborne, D. Bessinger, T. Bein, R. H. Friend, F. Auras, *J. Am. Chem. Soc.* **2019**, *141*, 15693–15699.
- [27] A. M. Evans, N. P. Bradshaw, B. Litchfield, M. J. Strauss, B. Seckman, M. R. Ryder, I. Castano, C. Gilmore, N. C. Gianneschi, C. R. Mulzer, M. C. Hersam, W. R. Dichtel, *Adv. Mater.* **2020**, *32*, 2004205.
- [28] P. Kuhn, M. Antonietti, A. Thomas, *Angew. Chem. Int. Ed.* **2008**, *47*, 3450–3453; *Angew. Chem.* **2008**, *120*, 3499–3502.
- [29] H. Qian, F. Meng, C. Yang, X. Yan, *Angew. Chem. Int. Ed.* **2020**, *59*, 17607–17613; *Angew. Chem.* **2020**, *132*, 17760–17766.
- [30] D. Stewart, D. Antypov, M. S. Dyer, M. J. Pitcher, A. P. Katsoulidis, P. A. Chater, F. Blanc, M. J. Rosseinsky, *Nat. Commun.* **2017**, *8*, 1102.
- [31] P. M. Hergenrother, *High Perform. Polym.* **2003**, *15*, 3–45.
- [32] Q. Fang, Z. Zhuang, S. Gu, R. B. Kaspar, J. Zheng, J. Wang, S. Qiu, Y. Yan, *Nat. Commun.* **2014**, *5*, 4503.
- [33] Q. Fang, J. Wang, S. Gu, R. B. Kaspar, Z. Zhuang, J. Zheng, H. Guo, S. Qiu, Y. Yan, *J. Am. Chem. Soc.* **2015**, *137*, 8352–8355.
- [34] L. Jiang, Y. Tian, T. Sun, Y. Zhu, H. Ren, X. Zou, Y. Ma, K. R. Meihaus, J. R. Long, G. Zhu, *J. Am. Chem. Soc.* **2018**, *140*, 15724–15730.
- [35] H. Veldhuizen, A. Vasileiadis, M. Wagemaker, T. Mahon, D. P. Mainali, L. Zong, S. Zwaag, A. Nagai, *J. Polym. Sci. Part A* **2019**, *57*, 2373–2377.
- [36] G.-Y. Lee, J. Lee, H. T. Vo, S. Kim, H. Lee, T. Park, *Sci. Rep.* **2017**, *7*, 557.
- [37] D. Jiang, *Bull. Chem. Soc. Jpn.* **2021**, *94*, 1215–1231.
- [38] J. Maschita, T. Banerjee, G. Savasci, F. Haase, C. Ochsenfeld, B. V. Lotsch, *Angew. Chem. Int. Ed.* **2020**, *59*, 15750–15758; *Angew. Chem.* **2020**, *132*, 15880–15888.
- [39] B. Baumgartner, M. J. Bojdys, M. M. Unterlass, *Polym. Chem.* **2014**, *5*, 3771–3776.
- [40] B. Baumgartner, M. Puchberger, M. M. Unterlass, *Polym. Chem.* **2015**, *6*, 5773–5781.
- [41] T. Kim, B. Park, K. M. Lee, S. H. Joo, M. S. Kang, W. C. Yoo, S. K. Kwak, B. S. Kim, *ACS Macro Lett.* **2018**, *7*, 1480–1485.
- [42] T. Osawa, T. Kajitani, D. Hashizume, H. Ohsumi, S. Sasaki, M. Takata, Y. Koizumi, A. Saeki, S. Seki, T. Fukushima, T. Aida, *Angew. Chem. Int. Ed.* **2012**, *51*, 7990–7993; *Angew. Chem.* **2012**, *124*, 8114–8117.
- [43] S. Yang, X. Li, Y. Qin, Y. Cheng, W. Fan, X. Lang, L. Zheng, Q. Cao, *ACS Appl. Mater. Interfaces* **2021**, *13*, 29471–29481.
- [44] M. Dogru, T. Bein, *Chem. Commun.* **2014**, *50*, 5531–5546.
- [45] K. Ariga, *Nanoscale Horiz.* **2021**, *6*, 364–378.
- [46] C. Zhang, S. Zhang, Y. Yan, F. Xia, A. Huang, Y. Xian, *ACS Appl. Mater. Interfaces* **2017**, *9*, 13415–13421.

Manuscript received: October 11, 2021

Accepted manuscript online: October 28, 2021

Version of record online: November 25, 2021